PAPER

Check for updates

Correlation between domain structure dynamics and electromechanical behavior in Sn-doped BaTiO₃

Viktoria Kraft, [iD] *[a] Maria Rita Cicconi, [iD] [a] Subhajit Pal, [iD] [b] Michel Kuhfuß, [iD] [a] Neamul H Khansur, [iD] [ac] Alexander Martin, [iD] [d] Koji Kimura, [iD] [e] Yasuhiro Takabayashi, [iD] [e] Ko Mibu, [iD] [e] Koichi Hayashi, [iD] [e] Joe Briscoe [iD] [b] and Kyle G. Webber [iD] [a]

Lead-free photoferroelectrics are promising for multimodal energy conversion systems that can harvest diverse ambient energy sources, including light and mechanical vibrations. When multiple physical phenomena are coupled within a single material, the ferroelectric, piezoelectric, and photoresponsive properties are strongly governed by the ferroelectric domain structure and domain wall mobility. To lay the groundwork for understanding such complex couplings, this study focuses on isolating and investigating the influence of the domain structure in Sn-doped BaTiO₃ ($BaSn_xTi_{1-x}O_3$) on its small-signal electromechanical behavior. Rayleigh analysis was carried out to study domain wall mobility as a function of Sn content up to 11 mol%, revealing the highest irreversible contributions around 11 mol% Sn. Additionally, domain types were investigated with spatially resolved Raman spectroscopy and piezoresponse force microscopy, and correlated with electromechanical properties. These results demonstrate that Sn doping modifies the domain sizes and shapes, impacting domain wall mobility and dielectric response. Understanding domain structure dynamics in relation to electromechanical behavior is essential for optimizing coupled photoferroelectric properties.

Introduction

One approach to address the growing energy demand for modular electronic devices is through the harvesting of ambient energy, in particular through so-called multimodal energy harvesting systems.[1–6] These systems benefit from the ability to convert multiple energy sources, such as mechanical, thermal, and solar energy. While this approach generally appears promising for addressing issues such as the absence of single sources like radiation, vibration, or heat,[7] these energy conversion systems often prioritize the continuous harvesting of energy from multiple sources rather than maximizing the energy conversion efficiency when compared to a single-source converter.[5,8]

[a] Department of Materials Science and Engineering, Friedrich-Alexander-Universität Erlangen-Nürnberg, Erlangen 91058, Germany. E-mail: viktoria.kraft@fau.de

[b] School of Engineering & Materials Science, Queen Mary University of London, London E1 4NS, UK

[c] Department of Materials Science & Engineering, Case Western Reserve University, Cleveland OH, 44106 OH, USA

[d] Department of Life Science and Applied Chemistry, Nagoya Institute of Technology, Nagoya, Aichi 466-8555, Japan

[e] Department of Physical Science and Engineering, Nagoya Institute of Technology, Nagoya, Aichi 466-8555, Japan

Significant progress towards multimodal energy harvesting systems has been made in the development of multi-material samples,[1,5,9] composites,[2,10–13] polymer-based systems,[2,9–11] thin films,[14,15] hydrogels,[3,11,16] and nanomaterial technologies,[2,4,10] among others. These advancements have led to extended applicability in areas such as neuromorphic computing,[17] antibacterial strategies,[10] neuromodulation,[18] flexible sensors,[16] body motion sensing and monitoring,[1,3,12,13] smart security systems,[2] wastewater treatment,[4] and beyond. Different strategies can be employed to engineer multimodal energy harvesters, for instance, different materials or converters can be combined to harvest various energy sources.[5] Alternatively, single-material systems, like $((K_{0.49}Na_{0.49}Ba_{0.02})(Nb_{0.99}Ni_{0.01})O_{2.995})$,[8] and Bi_2FeCrO_6,[14] have been shown to harvest multiple energy sources simultaneously. In the field of photo-electro-mechanical coupling, so-called photoferroelectrics have attracted significant interest.[8,19] Photoferroelectric phenomena include photostimulated phase transitions, illumination-induced phase transition temperature shifts, and photoinduced deformation arising from spontaneous polarization and electrostrictive changes.[20]

Barium titanate (BaTiO₃, BT), a photoferroelectric material,[8,21] becomes particularly viable for multimodal energy conversion through doping, e.g., $Ba_{1-x}(Bi_{0.5}K_{0.5})_xTiO_3$,[22] $Ba_{1-x}(Bi_{0.5}Li_{0.5})_xTiO_3$,[23]

and 0.5Ba(Zr$_{0.2}$Ti$_{0.8}$)O$_3$–0.5(Ba$_{0.7}$Ca$_{0.3}$)TiO$_3$ (BCZT),[24] or within a composite structure.[25] One dopant that has gained attention for its potential to improve multimodal energy conversion while enhancing the electromechanical properties of BT at room temperature is Sn (BaSn$_x$Ti$_{1-x}$O$_3$, denoted as BTSn100x).[26–28] This is due to the potential occurrence of coexisting crystallographic phases,[26,27,29,30] (comparable to BCZT[31]) in BTSn100x. This coexistence is made possible as Sn has the ability to shift the Curie point (around 127 °C for BT[32]), the tetragonal-to-orthorhombic (around 5 °C for BT[32]), and the rhombohedral-to-orthorhombic (around −90 °C for BT[32]) phase boundary toward room temperature.[33,34] By tuning the phase boundaries of BT, it is possible to shift the enhanced properties around phase boundaries to temperatures suitable for practical applications.[27,28,30] Furthermore, the appearance of polar nanoregions at higher Sn concentrations (≥10 mol% Sn) enhances the material's functional potential, persisting even beyond the Curie point into the paraelectric phase.[26,34–36]

As with most ferroelectric materials, the performance of BTSn100x is closely linked to its domain properties, particularly in relation to its ferroelectric and piezoelectric response.[37–39] Additionally, its photoelectric properties are also coupled to the ferroelectric (FE) domain state, further emphasizing the importance of understanding its domain properties.[40,41] Increasing the number of domain walls, for instance, can be utilized to enhance the photovoltaic response by increasing the photovoltage.[42] Further, it was shown that illumination can affect domain wall mobility, which in turn influences the overall ferroelectric response by altering the conductivity or introducing stress at domain walls.[43,44] However, the role of domain walls in photovoltaic efficiency remains under debate.[15,45,46] It should be noted that domain walls have mostly been studied as simple interfaces, but should be considered as more complex 3D structures embedded within the bulk of the material.[47] They are often investigated in terms of their mobility or interactions with defects rather than their intrinsic properties.[47] However, with growing interest in domain wall engineering, where domain walls are tuned to define the target properties of a material, a comprehensive investigation of domains is essential to advancing this field.

To understand the role of Sn in enhancing electromechanical response, it is crucial to correlate domain states with the previously investigated properties, such as the piezoelectric charge coefficient.[27,29,30] Previous studies, using piezoresponse force microscopy (PFM) for domain imaging and switching behavior,[35,48–50] scanning electron microscopy (SEM) for structural characterization,[35,51] and transmission electron microscopy (TEM) for high-resolution domain and defect visualization,[26,34,35,52] have provided valuable insights into BTSn100x. Incorporating spatially resolved Raman spectroscopy data could provide further understanding by offering additional phase information and revealing local structural distortions. One of the advantages of Raman spectroscopy lies in the high spatial resolution, and its ability to correlate structural changes within the sample through variations in the Raman signal.[44,53] Previous studies on ceramic materials have shown that Raman spectroscopy is highly sensitive to factors such as crystal structure,[54] temperature, residual and externally applied stress,[54,55] as well as local compositional changes,[54,55] and

therefore, it is a powerful technique for investigating bulk functional property changes, despite being inherently surface sensitive.[56,57] However, performing conventional Raman spectroscopy at only a few selected spots presents challenges in data interpretation,[53] since the Raman signal could be affected by factors such as thermal expansion or local heating during measurements,[47,58] chemical heterogeneity,[54] domain state changes,[56] or the coexistence of crystalline phases.[55,58] One approach to address these challenges is to map the Raman vibrational modes across larger sample areas, allowing for correlation with optical microscopy images (spatial) to track structural changes (spectral) within the sample and perform a spatially resolved analysis (referred to as a hyperspectral dataset).[53–57]

While Raman mapping can be used to image the domain state, the domain dynamics remain unanswered. Additionally, employing Rayleigh analysis of the relative permittivity of unpoled samples derived from subcoercive electric-field-dependent polarization loops provides deeper insights into the effects of Sn doping on polarization and domain wall mobility. Furthermore, studies on unpoled samples remain rare,[52,59] despite being essential for correlating domain dynamics with microstructural factors such as grain size. Overall, this combined approach provides a comprehensive understanding of the structural and functional relationships in BTSn100x, enabling further advancements in the design of future photoferroelectric materials for multimodal energy conversion systems.

Experimental methodology

Polycrystalline Ba(Ti$_{1-x}$Sn$_x$)O$_3$ (x = 0, 0.03, 0.07, 0.11) ceramics were produced using the solid-state reaction method with BaCO$_3$ (99.8% purity, Thermo Fisher Scientific), TiO$_2$ (99.6% purity, Thermo Fisher Scientific), and SnO$_2$ (99.9% purity, Thermo Fisher Scientific) powders. The starting materials were dried overnight at 120 °C and stoichiometrically weighed in a humidity-controlled glovebox (R_H < 15%). Subsequently, the mixture was homogenized by ball milling using yttria-stabilized zirconia and ethanol for 24 h. With a rotary evaporator under reduced pressure, the solvent was removed from the mixture, and after drying, calcination was performed at 1200 °C for 6 h (5 K min^{-1} heating and cooling rate). To achieve a homogeneous and fine particle size, the powders were again milled for 72 h. The dried powders were first formed into disks of 10.2 mm diameter and then cold isostatically pressed for 5 min under 180 MPa. The samples were sintered at 1380 °C for 4 h (5 K min^{-1} heating and cooling rate). With a surface grinder, the samples were machined to obtain discs with a thickness of 0.8 mm (±0.02 mm) for different electrical measurements, and thinner discs of 0.45 mm (±0.03 mm) for various imaging techniques. Additionally, the thin discs were polished with diamond suspension down to 1 μm grit, followed by a 0.25 μm oxide polishing suspension. To remove internal residual stress induced by the grinding and polishing steps, the samples were annealed at 400 °C for 4 h.

The phase purity and the crystal structure of both the calcined powder and sintered samples were evaluated with

X-ray diffraction (Bruker D8 ADVANCE Eco, Bruker AXS) using a Cu Kα source in Bragg–Brentano geometry at room temperature. The microstructure of thermally etched samples (5 min at 1200 °C) was recorded at seven different spots per composition with a scanning electron microscope (SEM, Quanta 200, FEI Co.). Over 350 grains were analyzed per composition to determine the average grain size and distribution with the help of an automated, commercially available image analysis software (MIPAR v5.0 with Spotlight Package, MIPAR Image Analysis).

To confirm the valence state and the local environment of Sn in the sintered samples, ^{119}Sn Mössbauer spectroscopy was performed at room temperature for sintered and subsequently crushed powder samples. A Pd foil filter and a NaI scintillation counter were applied to utilize the conventional absorption method. Randomness of the crystal orientation was achieved by mixing silicone grease into the sintered powders and applying it on pure Al foil. Ca^{119m}SnO$_3$ was utilized for the γ-ray source, and a standard α-Fe foil and CaSnO$_3$ powder were used for the velocity calibration. As the zero-velocity standard, the peak position of CaSnO$_3$ was chosen.

Sn K-edge X-ray absorption fine structure (XAFS) measurements were performed for Ba(Ti$_{1-x}$Sn$_x$)O$_3$ (x = 0.03, 0.07, 0.11) at BL14B2 in SPring-8, Japan. The data were measured in transmission mode at 300 K using two ionization chambers in front of and behind the sample. The incident X-rays were monochromatized with a double Si (111) crystal. The XAFS spectrum of a Sn foil was used to calibrate the incident X-ray energy, and the first inflection point of the foil spectrum was set to 29.200 keV. The extended XAFS (EXAFS) oscillations $\chi(k)$ were extracted from the raw absorption spectra using the Artemis software package.[60] Then, $k^3\chi(k)$ were Fourier transformed to obtain the radial distribution function $|F(R)|$. To obtain the oscillations of the nearest and second-nearest neighbors, the inverse Fourier transformation of the corresponding area of $|F(R)|$ was performed. Then, the obtained $k^3\chi(k)$ was fitted by the theoretical formula of XAFS oscillations to evaluate the interatomic distances around Sn.

Field emission scanning electron microscopy (FESEM, ULTRA Plus, Carl Zeiss SMT AG, Germany) combined with energy-dispersive X-ray spectroscopy (EDS, acceleration voltage of 15 kV) was used to collect microstructure images with elemental distribution maps. The samples were prepared by polishing with P1200 and P2000 abrasive papers, followed by a final finishing using a diamond suspension containing 1 μm-sized grains (Struers, France). The polished surfaces were coated with carbon.

Piezoresponse force microscopy (PFM) images were collected using a Bruker Dimension Icon AFM instrument. The measurements were performed with a SCM-PIT-V2 probe (spring constant = 3 N m^{-1}, sensitivity = 63 nm V^{-1}) with a 2 V AC bias at the contact resonance frequency. Calibration of the instrument phase offset was done with a standard BaTiO$_3$ single crystal. 2D FFT of the PFM image is performed using Gwyddion software.

Unpolarised Raman spectra were measured in the frequency range of 80–1250 cm^{-1} using an alpha300R Raman microscope (WITec, Oxford Instruments) equipped with a 532 nm laser, a high-quality microscope with Zeiss EC Epiplan-Neofluar objectives, and a fiber-coupled ultra-high throughput (UHTS) spectrometer (grating 1800 g mm^{-1}). A 50×/0.75 objective was used, providing a spatial (lateral) resolution of less than 1 μm and a depth of focus of the light cone of ∼ 3.8 μm (sampling volume: $4n\lambda/NA^2$, with n =1). Depending on the sample grain size, an area of 240 × 240 μm^2 or 120 × 120 μm^2 was mapped with a step of 1 μm, resulting in a very high number of spectra collected ($> 10\,000$). Each spectrum is associated with a spatial position (x–y coordinates), a spectral position (cm^{-1}), and an intensity (counts per second). The entire hyperspectral dataset was background-subtracted with a linear function and normalized to the total area. Data analysis of the Raman area maps was done using the Witec Project software (version 7.0), which allows multivariate image generation by using the information of the entire hyperspectral dataset to create color-code contour images.[56] For the data analysis, the barycenter position (or centroid) of the [TiO$_6$] stretching frequency region (∼450–650 cm^{-1}; see SI, S1) was selected.[61] Furthermore, the multivariate tool true component analysis was used to identify the most different spectra in the dataset and to represent their spatial distribution in color-coded images.

For the electrical measurements, the circular parallel sides of the disks were sputtered with Pt electrodes (sputter coater Q 150T S plus, Quantum Design). Subcoercive polarization–electric field hysteresis loops were recorded at room temperature using a piezoelectric analysis system (TFAnalyzer 2000, aixACCT Systems GmbH). During measurements, 5 cycles with bipolar waveform at a frequency of 10 Hz were recorded for an applied maximum electric field of 2 to 280 V. For electric fields below 0.3 kV cm^{-1}, the internal amplifier of the aixACCT system was used, and for electric fields above this, a high voltage power amplifier (Model 20/20C, Trek) was required. For the Rayleigh analysis, the error ranges were obtained by determining the standard deviation of the linear fits for the reversible and irreversible contributions of each sample, and then, using error propagation, calculating the standard deviation of the percentage of the irreversible contributions.

Results and discussion

To investigate the influence of crystal structure on domain-related properties, XRD measurements were performed on sintered samples at room temperature over the 2θ range of 20°–80° (Fig. 1). The incorporation of Sn into the crystal lattice can be confirmed by a lower 2θ shift and broadening of the 111$_{pc}$ reflection (Fig. 1b), as expected due to the difference in ionic radii between Ti^{4+} (0.605 Å) and Sn^{4+} (0.69 Å),[62] with no secondary phases visible (Fig. 1a). Further, the split 200$_{pc}$ reflections become a more symmetric single reflection with increasing Sn content, indicating a change in the crystal phase (Fig. 1c). According to our previously reported phase diagram and dielectric data, the room-temperature phases of the samples are as follows: BT = O (orthorhombic) − T (tetragonal) boundary, BTSn3 = O, BTSn7 = R (rhombohedral) − O boundary, BTSn11 = R.[28] Phase coexistence occurs near phase
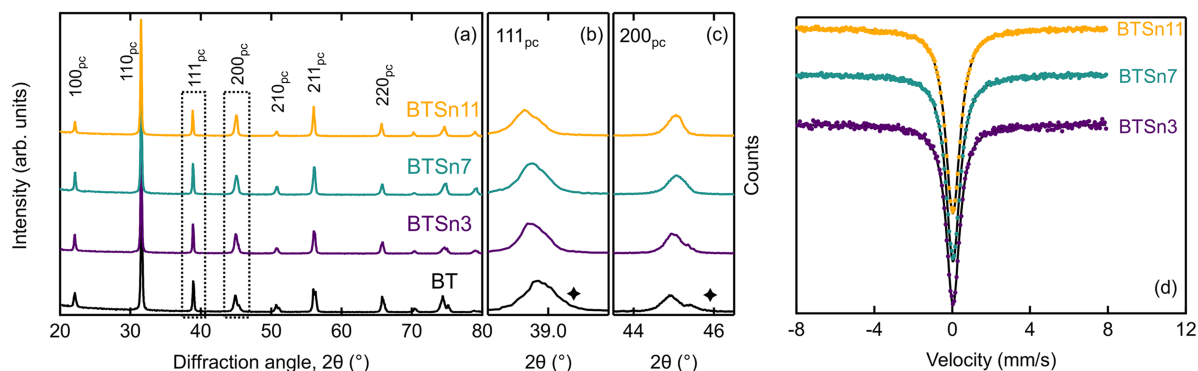
Fig. 1 Room temperature X-ray diffraction measurement of sintered BTSn100x with (a) the full measurement range and the enlarged reflections (b) 111$_{pc}$, and (c) 200$_{pc}$ (pc:pseudo-cubic). The Kα_2 contribution is marked with a star. ^{119}Sn Mössbauer spectroscopy (d) with Lorentzian fit (black) of sintered and crushed sample, revealing a Sn^{4+} oxidation state.

boundaries[48] and in Sn compositions of around 11 mol% and higher, depending on the temperature.[26,27,29,30] Different crystallographic phases and their coexistence can lead to changes in domain shape, number, and size, which can influence not only the domain structure but also the domain dynamics.

The unit cell volume, determined using a single *P4mm* space group, shows a general increase with higher Sn content: BT: 64.355 Å^3, BTSn3: 64.466 Å^3, BTSn7: 64.473 Å^3, BTSn11: 64.839 Å^3. This unit cell volume growth reflects an increase in structural symmetry and suggests a corresponding decrease in the lattice distortion and, by extension, a degradation in the reversible contributions to the electromechanical properties, which we also showed by measuring the stress-amplitude dependent piezoelectric coefficient.[28] Furthermore, the c/a ratio decreases from BT: 1.0102, BTSn3: 1.0073, BTSn7: 1.0053, BTSn11: 1.0043, supporting the trend toward a more symmetric structure. Hence, increasing the Sn content appears to lead to unit cell expansion, which reduces the tetragonal distortion, and therefore indicates a substitution on the B-site of BT. This means that approaching a higher-symmetry crystal phase through Sn doping is expected to influence functional properties such as spontaneous polarization, strain, coercive field, and stress, as well as domain switching behavior, among others.[63,64]

In order to verify the oxidation state of the Sn-dopants, Mössbauer spectroscopy was performed on the sintered samples. Here, data exhibits only a narrow and sharp single absorption, which was fitted with a single Lorentzian curve. By increasing the Sn content, no changes in signal width (0.96 ± 0.03 mm s^{-1}), peak positions (0.03 ± 0.01 mm s^{-1}), quadrupole splitting (0.00 mm s^{-1}), or appearance of additional shoulders are visible. This confirms that Sn retains its +4 oxidation state even after sintering, consistent with the oxidation state in the calcined samples as previously reported.[28] A change in oxidation state would affect local bonding, dipole displacement, polarization behavior, and consequently domain shape and dynamics.[65] These structural and chemical variations are especially sensitive to Raman spectroscopy,[55] which is utilized later in this study.

Similar to the data reported above from Mössbauer spectroscopy, XAFS measurements on calcined powders also hint towards a constant oxidation state of Sn^{4+} within the examined concentration range (Fig. S1). In general, if Sn^{2+} were present

instead of Sn^{4+}, its larger ionic radius would be expected to cause a more pronounced increase in bond lengths.[66] These changes in bond distances would have been indicated by a shift in peak position as a function of Sn content. However, no such shift is observed here. It should be noted that the bond lengths of Sn–O and Sn–Ba were observed to be larger than those of Ti–O and Ti–Ba, respectively, reflecting the increase in ionic radii from Ti^{4+} to Sn^{4+}. The obtained bond length values are in good agreement with those previously reported in literature for 3 and 11 mol% Sn (Fig. S1c, d and e). In general, XAFS has the potential to reveal concentration-dependent local structural changes and chemical heterogeneities. Interestingly, the amplitude of the high-frequency components in EXAFS spectra is slightly larger for the 3 mol% Sn sample than for the 7 and 11 mol% Sn samples, as shown in Fig. S1b. This trend indicates that interatomic correlations beyond the first coordination shell become weaker with increasing Sn substitution.

Moreover, EDS maps were collected and correlated with FESEM images (Fig. S2) to provide insight into the elemental distribution across the samples. The EDS maps show that all elements are homogeneously distributed throughout the mapped areas, including different grains and their boundaries. No regions with elemental accumulation were observed. Therefore, it is assumed that changes in domain morphology with Sn content are likely not primarily due to local compositional variations within the sample.

In addition to crystal structure, the microstructure also influences electromechanical properties, particularly in relation to domain wall structure, dynamics, and their interactions.[35,67] For Sn-doped BT, it is generally reported that grain size decreases with increasing Sn content,[30,48] although this trend is reversed in the case of nanometer-sized powders.[68] Fig. 2 shows representative microstructure images and histograms of the analyzed grains, including normal distributions and median (d_{50}) values. A reduction of nearly 50% in the d_{50} value from undoped BT (56 ± 41 µm) to doped samples (BTSn3: 26 ± 19 µm, BTSn7: 26 ± 18 µm, BTSn11: 19 ± 13 µm) can be observed. Up to the tested concentrations, a decrease in grain size was observed with increasing Sn content. This is important to note, as grain size strongly affects domain size, width, and
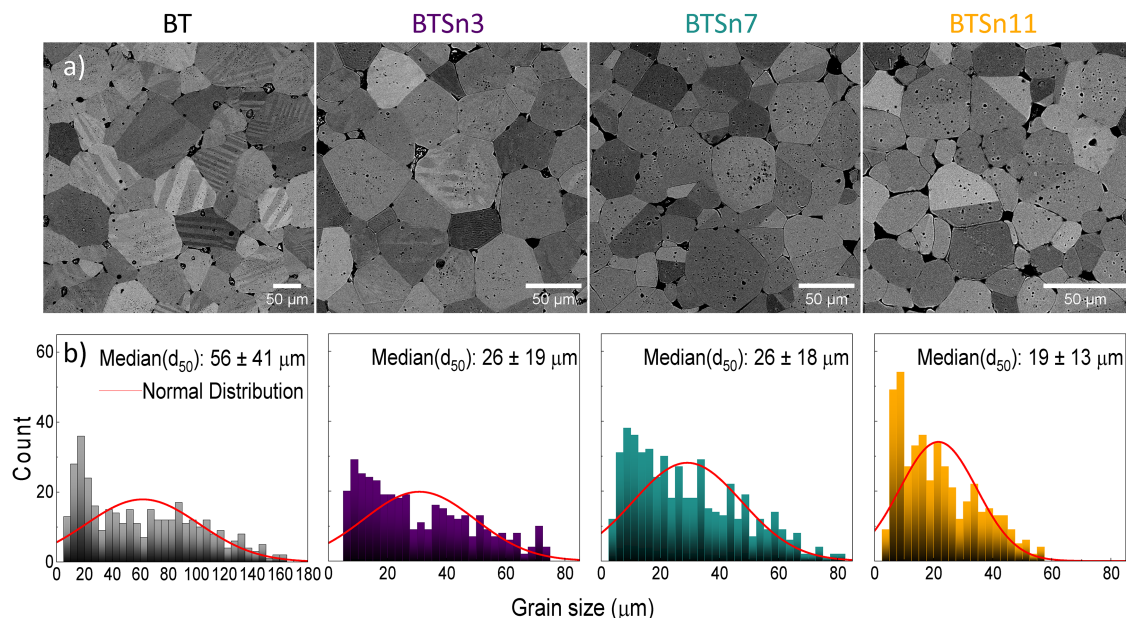
Fig. 2 (a) Scanning electron microscope images, and (b) grain size distribution and d_{50} values of BTSn100x samples.

density.[67] A complementary approach to clarify purely the influence of microstructure on functional properties would be to compare samples with different grain sizes at a fixed Sn concentration,[35] as has been done for BT.[69] Importantly, density measurements of the sintered samples using the Archimedes method showed an increase with Sn content, with relative densities exceeding 95%. Large pores within and between the grains were observed, which could be attributed to the presence of oxygen and barium vacancies, among other factors.[70]

The typical stripe-like, lamellar domains observed in undoped BT, characterized by alternating a- and c-type domains,[71] are visible, consistent with previous reports for coarse-grained BT.[51] These domains are reported to be 90° domains, occurring below the Curie point for internal stress reduction.[72] A few grains show that more than one type of domain orientation can be found within one grain, which probably occurs due to the coalescence of grains.[71] Some stripe-like domains are still observable in BTSn3, where Sn may disrupt them into domain islands by increasing chemical heterogeneity.[35] With increasing Sn content, the large laminar domains are no longer visible. Furthermore, the visibility of smaller domain structures may be hindered by changes in domain shape and the presence of pores. Due to the resolution limits of the measurement apparatus, PFM was used to gain further insight.

The evolution of domain shapes in BT with Sn doping was studied using PFM and is presented in Fig. 3. The measured undoped sample predominantly exhibits lamellar-type domains.[50] With increasing Sn content, these domains gradually transform into more complex configurations, as indicated with the schematic diagram in Fig. S3a. At low Sn concentrations, such as 3 mol%, lamellar domains are clearly visible,[35,50] while higher concentrations lead to the additional appearance of watermark-like,[50,51] and herringbone patterns[50,72] (compare Fig. S3b), eventually transitioning into nanodomains and polar nanoregions

(PNRs) above 15 mol% Sn.[50] Interestingly, with techniques such as TEM, it is possible to observe nanodomains even in at 11 mol% Sn.[26] Sn doping is known to disrupt long-range ferroelectric order[49,50] and induce local lattice distortions,[48,58] thereby altering domain morphology. This gradual transition complicates the determination of domain width and density, particularly when multiple domain types coexist within a single composition. A statistically meaningful value would require analysis of a large number of domains across numerous sample spots; therefore, absolute values were not determined here.

The PFM studies on BT, BTSn3, 7, 11 show the materials consisting of both in-plane and out-of-plane domain configurations. However, BTSn7 exhibits a significantly different and relatively smaller domain structure, whereas BTSn3 and BTSn11 appear more similar to each other. The pattern of the domain structure in these materials can also be understood by performing the 2D FFT of the amplitude response. This method analyzes the distribution or anisotropy in the materials. For example, it is a well-established technique used to study nanodomain distributions in relaxor systems,[73] which cannot be assessed only from the PFM image. The radial sum intensity analysis over 360° enabled evaluation of domain periodicity, orientation, and defect structures. The 2D FFT distribution in BT shows a uniform pattern with bright spots from stripe-like and periodic domain types. In contrast, BTSn3 and BTSn11 display anisotropy, as indicated by the arrows, while BTSn7 shows a uniform elliptical distribution. Jiang et al.[48] investigated 7.5 mol% Sn-doped samples and reported contrast differences in phase images corresponding to orthorhombic and tetragonal crystal structures. The observed differences in amplitude image contrast were attributed to varying piezoelectric properties, with orthorhombic phases exhibiting stronger responses, which is consistent with the enhanced properties observed for BTSn7 within the orthorhombic phase, when comparing the response of the different crystal phases. Additionally, they observed localized contrast changes near
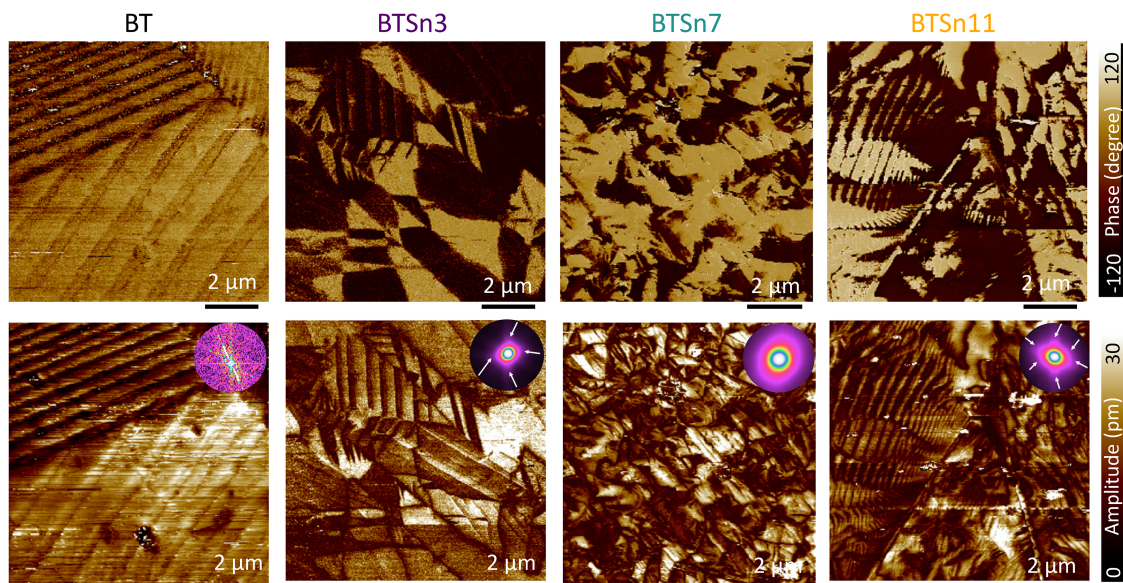
Fig. 3 Comparison of representative piezoresponse force microscopy amplitude and phase images of BTSn100*x*, with 2D fast Fourier transform of the amplitude image and the arrows representing anisotropy.

phase boundaries, likely due to local stress and resulting spatial inhomogeneities. Such proximity to phase boundaries is known to enhance electromechanical properties, consistent with the highest piezoelectric coefficients observed for BTSn7 at room temperature.[28] Moreover, the transition toward smaller, more intricate domain structures is critical for optimizing electromechanical performance, particularly by affecting domain wall mobility.

In addition to variations in the domain structure with composition, the grain size also plays an important role. Herringbone-type domains, for example, are typically found in coarse-grained tetragonal BT, while stripe-like domains are found in fine-grained samples.[51] The overall domain width of pure BT is known to decrease with decreasing grain size.[51] Similar trends can be found in doped BT. For example, Tan *et al.*[51] investigated 4 mol% Sn-doped samples and found that smaller-grained ceramics ($\sim$0.8 μm) exhibited mosaic-like domain structures and potential polar nanoregions (PNRs), resembling relaxor ferroelectrics, likely forming multi-domain configurations within single grains. In contrast, larger-grained samples ($\sim$8.5 μm) in the study of Tan *et al.*[51] showed stripe-like domains, similar to those observed in our BTSn3. However, the grain size of our BTSn3 is approximately three times larger ($\sim$26 μm), which can be attributed to different processing conditions and starting materials. These observations are similar to the domain structure evolution with increasing Sn content, highlighting the coupled effect of Sn concentration and grain size on domain morphology and, consequently, electromechanical behavior.

Similar to the PFM-based observations, room-temperature Raman area maps also revealed changes in domain morphology with Sn doping. The sample surface was first examined using optical light microscopy (Fig. 4a), providing an overview of grain dimensions, grain boundaries, and macroscopic features such as

pores to guide the selection of the region to map. Since BT possesses nearly twice the grain size compared to Sn-doped samples, different magnifications were selected to appropriately capture the area of different grains and their boundaries for all compositions.

For BT, a typical Raman spectrum of the tetragonal phase is shown in Fig. S4, while the main Ti-related vibrational modes are reported in Table S1, with their assignment, based on previous reports.[44,58] In brief, the spectrum in Fig. S4 shows relatively broad vibrations representing stretching of the $\langle$Ti–O$\rangle$ bonds in [TiO$_6$] octahedra as well as bending modes of the Ti–O–Ti bonds. The main discernible Raman vibrations are transverse (TO) and longitudinal (LO) modes at $\sim$180, 270, 307, 470, 510, and 715 cm^{-1}. For clarity, we will refer to three main frequency regions: the low-frequency region (LF) from 100 to $\sim$450 cm^{-1}, the intermediate frequency region (IF), between $\sim$450–650 cm^{-1}, and the high frequency (HF) region from $\sim$680 to $\sim$850 cm^{-1}. The relative intensity of the modes in the three frequency regions changes depending on symmetry, but also on crystallographic orientation, as clearly shown in BT single crystals.[44,74] In particular, the Ti–O stretching mode in the IF region shows strong changes depending on the orientation, with the suppression or enhanced intensity of the mode around 470 cm^{-1}. To represent these variations over a large area, we used the barycenter (or centroid) of the IF stretching modes (ref. 61, see also inset in Fig S4). Fig. 4b shows the spatial distribution of the IF region barycenter, reflecting relative changes in the Raman Ti–O stretching modes within the mapped area. For instance, in BT, the barycenter changes from 529 to 535 cm^{-1}, corresponding to the darkest and brightest colors in Fig. 4b, respectively. The barycenter variation across the mapped area follows specific periodic patterns, and highlights the presence of regular "intra-grains"
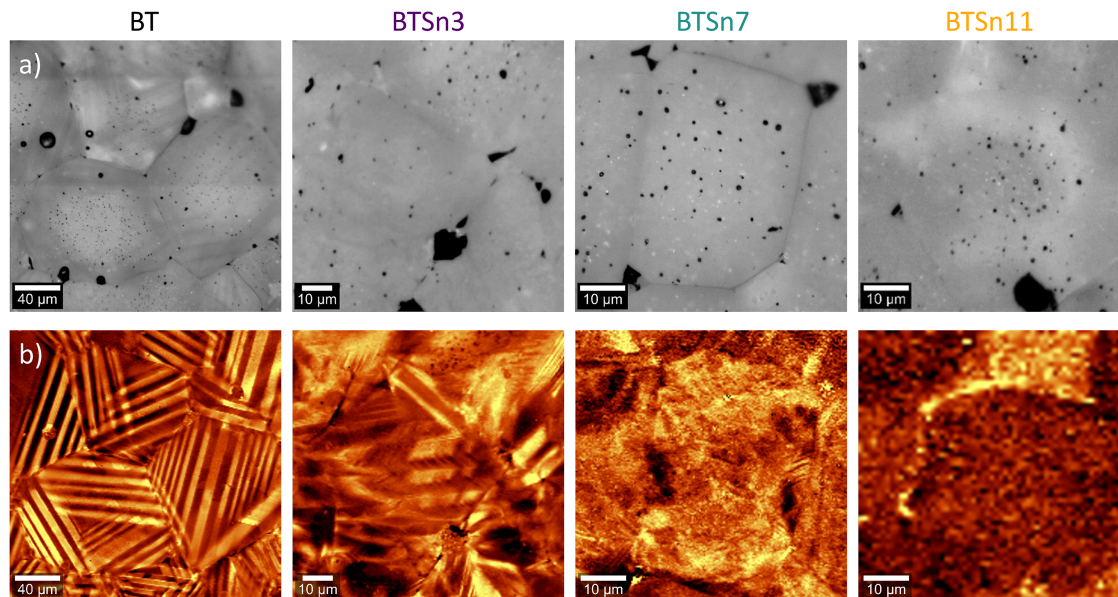
Fig. 4 (a) Optical light microscopy images of BTSn100x samples showing the surface of the samples and (b) reconstructed Raman imaging of the spatial distribution of the barycenter, highlighting the presence of various domain types and sizes of the same investigated sample area. The brightest colors represent a shift of the barycenter toward higher frequencies.

lamellar-type domains. With increasing Sn content, the relative variation in barycenter position within the mapped areas decreases (BTSn3: 10 cm^{-1}; BTSn7: 5 cm^{-1}; BTSn11: 4 cm^{-1}), while the intra-grains periodic features become more complex before eventually disappearing. Although the spatial resolution is limited to the micrometer range and mainly captures large-scale domains, the gradual transition from lamellar domains in BT to more complex configurations in doped samples remains visible. For instance, in BTSn3, some periodic step-like domains can be observed, while in BTSn7 and BTSn11, distinct domain structures are no longer resolved at this magnification. This agrees well with the PFM data in Fig. 3 where the domain size is well below the micrometer range (below around 1 μm).

To gain a deeper understanding into the structural changes, the hyperspectral dataset was analyzed by determining the minimum number of distinct Raman spectra (components) required to reconstruct the full area. The spatial distribution of the different components is visualized as color-coded images in Fig. 5a. In BT, three signals, with distinct vibrational modes were identified, and represented, in the color-code map as red, blue, and green, respectively. Based on the studies done on BT single crystals,[44,74] it is possible to link different crystallographic orientations with the relative intensity change or suppression of specific vibrations: the ∼470 cm^{-1} mode and the HF mode around 715 cm^{-1}. For example, in the red Raman spectrum of BT (Fig. 5b), there is no evident 470 cm^{-1} vibration, and at the same time, the 715 cm^{-1} mode is damped. In contrast, the blue spectrum has both, with a particularly intense HF vibration. These specific features, and their relative changes, are consistent with different crystallographic orientations identified in the BT single crystal, and referred to as a- and c- domains, respectively.[74] The a-type domain is distinguished from the c-type by the absence of the Raman modes around 470 cm^{-1} and

715 cm^{-1}.[44] The third component (green spectrum) identified in BT is an intermediate spectrum between the blue and the red, and its origin could derive from (i) another c-domain with a slightly different orientation, (ii) a mixed signal originating from the presence of both red and blue components (domains smaller than the spatial resolution), (iii) an a domain boundary as reported for BT single crystal.[44]

In comparison, for the Sn-doped samples, only two distinct spectra were identified. For both BTSn3 and BTSn7, the spectra with the red colour show similarity with the BT a-domain (absence of the 470 cm^{-1} mode and damped signal in the HF region), while the blue components show similarities with the BT c-domain. While these two samples show similar trends in the presence and absence of the modes of interest, a domain structure correlation was only possible for BTSn3, since in BTSn7 the distinct patterns can no longer be clearly resolved, which also applies to BTSn11. In particular, in the latter, even the most distinct spectra reported in Fig. 5b no longer display discernible differences in any frequency region, and the greatest variations occur between different grains. Interestingly, with increasing Sn content, the reduced correlatability of microstructural features with the Raman response is consistent with the decreasing variation in barycenter position, as discussed above.

Additionally, the average domain wall density was estimated for BT from the different microscopy techniques used (Fig. S5–S7) for comparison (Table S2). The average density was calculated by dividing the number of visible stripe-like domain walls by a defined area.[75] The results show that the average domain wall densities obtained from SEM and PFM are comparable, whereas those from the Raman maps are two orders of magnitude lower. The Raman imaging technique, as discussed above, does not provide sufficient resolution to capture the same number of domain walls as the other two methods. This becomes evident
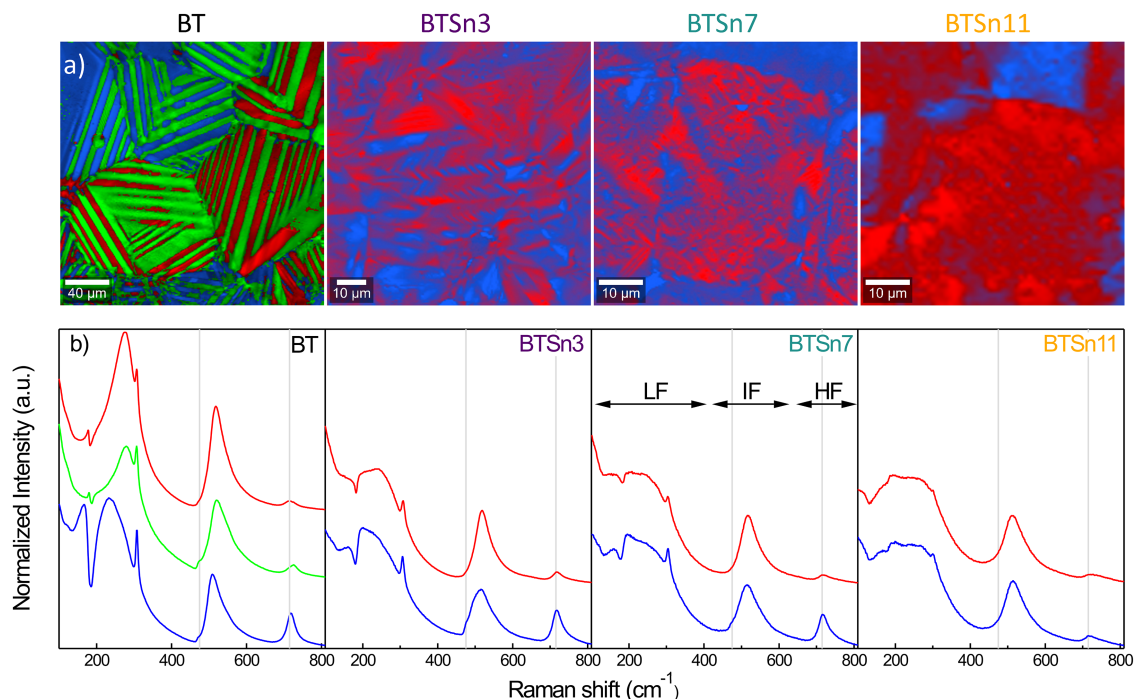
Fig. 5 Analysis of (a) the overlaid Raman maps and (b) the corresponding normalized Raman signal for the different components, Sn content-dependent.

in Fig. S8, which shows domain wall density as a function of measured area, where the density decreases with larger sampled areas due to reduced spatial resolution and magnification. While large macroscopic domains are still visible in the Raman images, smaller intra-domain structures, clearly resolved in the SEM image in Fig. S6, can no longer be distinguished. These differences in average domain wall density emphasize the importance of combining multiple imaging techniques. Hence, to achieve a comprehensive understanding of domain structure evolution, Raman mapping alone is not sufficient, particularly for high Sn content samples such as BTSn11. Therefore, PFM images of BTSn11 domains are crucial.

To gain insights into structure–property relationships, specifically the role of domain wall dynamics, Rayleigh analysis of the ferroelectric response was performed to understand the reversible and irreversible contributions to the measured real permittivity. For this purpose, the ferroelectric polarization response was recorded. Fig. 6a shows the large signal electric field (above the coercive field, E_c) hysteresis loops of the samples at RT, revealing clear domain switching behavior. Overall, a reduction in E_c with increasing Sn content is observed (BT, BTSn3, BTSn7, and BTSn11, of 2.61, 1,48, 1.19, and 0.53 kV cm^{-1}, respectively). Additionally, the hysteresis loops become slimmer, reflecting the transition toward relaxor-like behavior, as frequently reported in the literature.[33,49,50] The remnant polarization P_R initially increases from BT to BTSn3, likely due to the proximity of BT to the O–T phase boundary. These boundaries coincide with the sharp slope changes observed earlier in the temperature-dependent dielectric analysis.[28,76] However, beyond BTSn3, the P_R decreases with further Sn doping, consistent with the trend in

the calculated reduction of spontaneous polarization P_S,[77] and transition towards a material with relaxor-like characteristics.

To analyze domain wall dynamics more specifically, the polarization–electric field response sub-coercive field measurements were investigated. Fig. 6b shows representative sub-coercive field hysteresis loops for the different compositions. A nonlinear and hysteretic response is still observable at low fields, particularly in BTSn11. With increasing Sn content, a stronger increase in polarization at lower electric fields becomes visible, which can be attributed to the reduced coercive field E_c resulting from Sn doping. This is expected to increase the extrinsic contributions at constant electric field values. To describe the polarization behavior *via* the Rayleigh law, the permittivity data are extracted and analyzed.[78]

Fig. 7 shows the calculated real ε' and imaginary ε'' permittivity of the different samples from the sub-coercive polarization–electric field loops (Fig. 6b). For the analysis of domain wall dynamics, in the following, only the sub-coercive field range, typically $E_c/2$,[78] will be necessary. However, the electric field range to investigate ε' and ε'' here was chosen based on the E_c of BT, the composition with the largest E_c. This approach, rarely applied and not yet reported for Sn-doped BT, ensures consistency across all compositions, improves comparability, and allows to observe differences in material behavior arising from Sn doping in response to the electric field. As a result of selecting this electric field range, domain switching for the Sn-doped samples, which have a lower E_c than BT, falls within the measured range and is therefore visible in the dielectric response. The ε' was calculated using the relation $\varepsilon' = (\varepsilon^{\star 2} - \varepsilon''^2)^{1/2}$, the ε'' was obtained from $\varepsilon'' = (A_E/\pi E_P{}^2)/\varepsilon_0$, and the complex permittivity
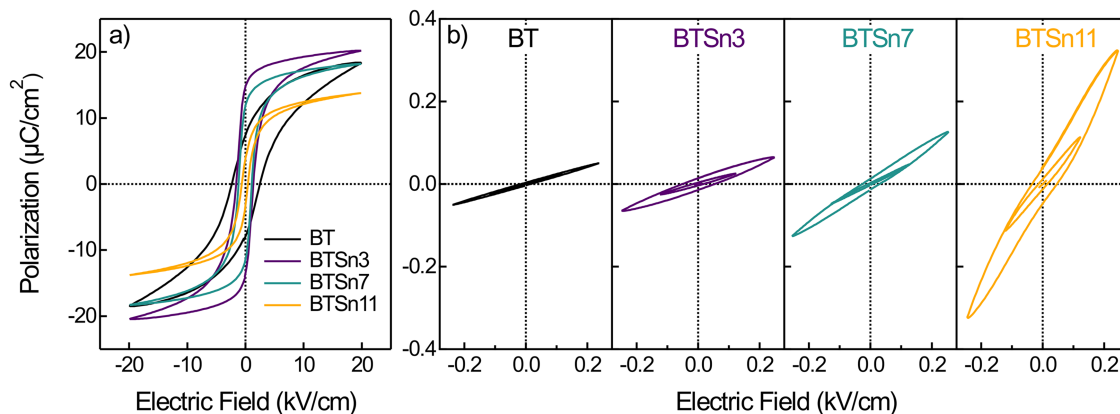
Fig. 6 Polarization electric field hysteresis loops at room temperature and 10 Hz with (a) at large electric fields (2 kV mm^{-1}), and (b) at representative sub-coercive electric fields.

ε^* was calculated from $\varepsilon^* = (P_{P-P}/2E_P)/\varepsilon_0$ with the loop area A_E, peak of the applied electric field amplitude E_P, the permittivity of free space ε_0, and the peak to peak polarization P_{P-P}.[78] Below E_c, all samples show a nonlinear increase in ε', which could be correlated with irreversible domain switching and domain nucleation events.[79] Interestingly, BT and BTSn3 exhibit a more gradual increase in this electric field range in both ε' and ε'', whereas BTSn7 and BTSn11 show a peak. Possible reasons for this behavior in this Sn concentration range include the reduced E_c, smaller domain size, i.e., higher domain wall density, increased polarizability and switchability, and enhanced dielectric response. The E_c shifts with increasing Sn content from a location at the rise of the dielectric data for BT and BTSn3, whereas for BTSn7 and BTSn11 it was found in the vicinity of the peak dielectric response.

Furthermore, the lattice contributions should typically be reduced with high electric fields, because the electronic and ionic contributions saturate.[80] For the Rayleigh analysis, only the linear region of the ε' below 0.3 kV mm^{-1}, based on $< E_c/2$ of BTSn11 (the sample with the smallest E_c), was used.

The analyzed region and corresponding linear fits are shown in Fig. 8a. The linear relationship $\varepsilon' = \varepsilon'_{init} + \alpha E_P$ was used to extract the Rayleigh coefficient α,[78,81] which provides insight into the irreversible contributions to the real permittivity, such as irreversible electric field-induced domain wall motion, phase transitions, and lattice strain. Under an applied electric field, irreversible domain wall motion may occur through domain wall pinning.[82,83] Further, it is known that both non-180° and 180° domain wall motions play a role in the dielectric
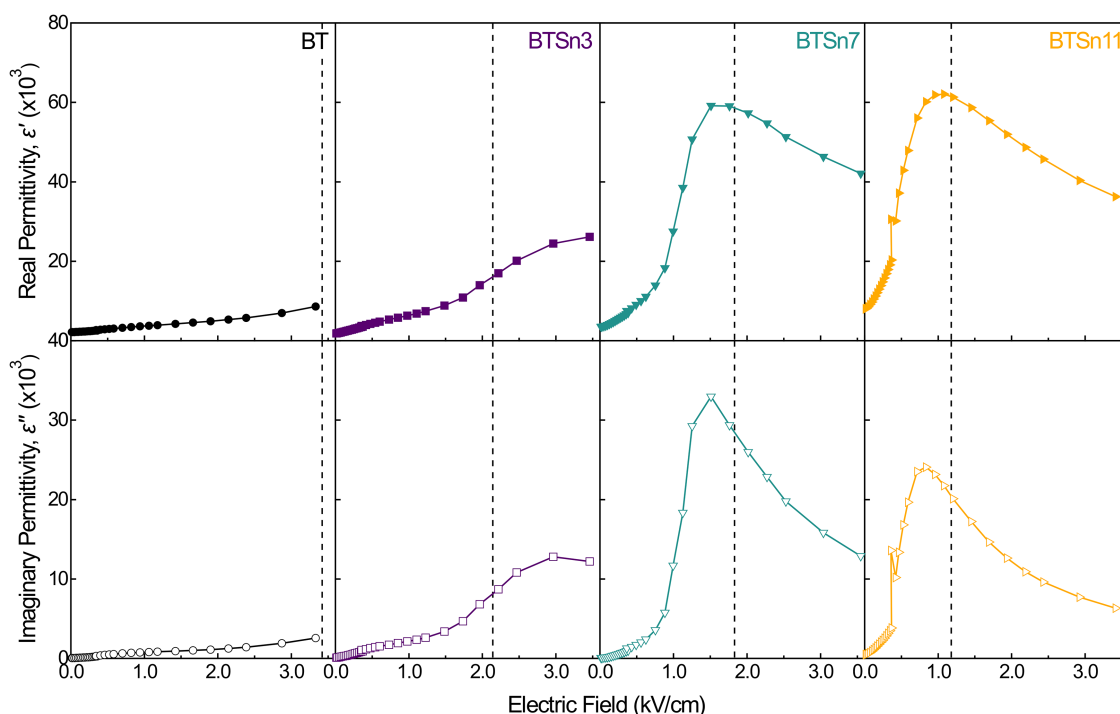

Fig. 7 Electric field dependent real permittivity ε' and imaginary permittivity ε'', calculated from polarization electric field hysteresis (at 10 Hz) with respective coercive filed E_c (dashed lines, measured at 20 kV cm^{-1}), Sn-content dependent.
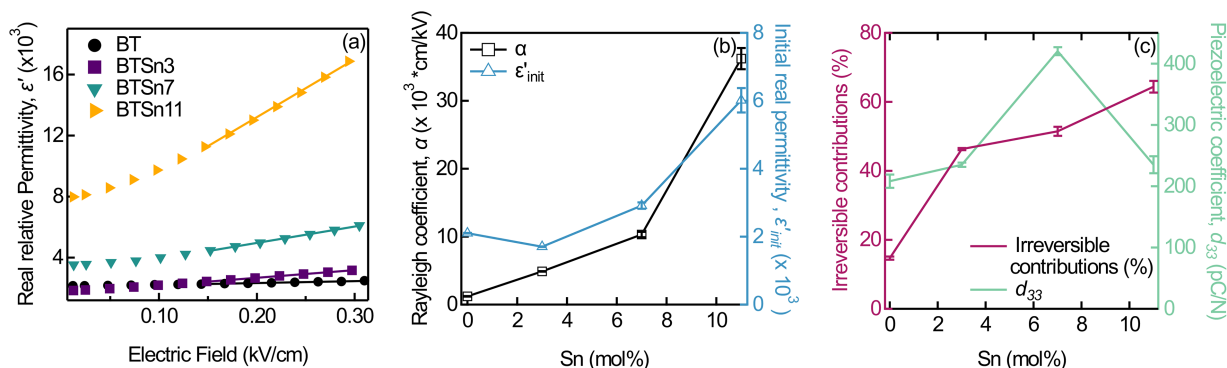
Fig. 8 Rayleigh analysis with (a) the linear fits of the Rayleigh region at low electric field amplitudes (0.15−0.3 kV cm^{-1}), (b) the extracted Rayleigh coefficient α, and initial permittivity $\varepsilon'_{\mathrm{init}}$, and (c) the percentage of irreversible contributions Sn-content dependent. The error bars are based on standard deviation.

response.[78] α increases with rising Sn concentration, which correlates with the observed decrease in E_{c}. A lower E_{c} implies a higher mobility of domain walls, which allows them to respond to lower electric field levels. Furthermore, the complex interplay between domain size, domain density, E_{c}, and the overall polarizability needs to be considered, which are all modified by increasing Sn content. With Sn doping, the domain size is reported to decrease while the domain density increases.[34] Additionally, both E_{c} and polarization are reduced, which enables an increase in α. Furthermore, an increase in domain wall clamping due to the reduced average grain size may explain this trend, which is consistent with earlier studies in the average grain size range of 0.5 to 5 µm.[84] The increase in α with Sn-content correlates well with the continuous transition in domain structures observed in PFM images and Raman maps, where the increased complexity in domain shape appears to influence the irreversible contributions. The increase in complexity is most likely due to increased local chemical inhomogeneity, caused by the incorporation of Sn. In NKN-based ceramics,[85,86] the formation of similar complex domains enhanced the irreversible contribution. It should be noted that ferroelectric response is further influenced by factors such as domain wall mobility, defect concentration, and space charges.[84]

The $\varepsilon'_{\mathrm{init}}$ at zero electric field reflects the reversible contributions, including unit cell deformation, reversible domain wall motion, and phase transitions. The evolution of α and $\varepsilon'_{\mathrm{init}}$ with Sn content is shown in Fig. 8b. Similar to the α, the $\varepsilon'_{\mathrm{init}}$ increases with higher Sn concentrations. This trend suggests that reversible contributions to the dielectric response become more significant in high Sn-content samples, which can rather be described as pseudo-cubic at RT. The increased symmetry in these compositions reduces lattice strain, enhancing switching behavior.[79,87,88] Furthermore, maximized $\varepsilon'_{\mathrm{init}}$ values were reported around 11 mol% Sn close to the Curie point located near the phase coexistence region.[52,59]

It is possible to further calculate the percentage of irreversible contributions from the Rayleigh analysis with $\alpha E_{\mathrm{P}}/(\varepsilon'_{\mathrm{init}} + \alpha E_{\mathrm{P}})$.[89] This percentage in Fig. 8c (pink line) also increases with rising Sn content, reaching the highest value at 11 mol%. The decreased domain size with increasing Sn content, as mentioned above, should also enhance the domain

and domain wall motion and therefore should be able to be correlated with the increase in the percentage of irreversible contribution. When comparing this percentage with previously reported piezoelectric coefficient d_{33} at room temperature, an increase in both values until 7 mol% Sn (Fig. 8c green line) can be observed. For BTSn11, a deviation occurs, while the percentage further rises, the d_{33} drops. BTSn11 has the highest α and $\varepsilon'_{\mathrm{init}}$ therefore should have the largest domain wall motion and the highest d_{33}. However, we must also separate between the direct and indirect piezoelectric effect. BTSn11 has the lowest P_{R} and the Curie point closest to room temperature, which also enhances back-switching of the sample and favors the indirect piezoelectric effect. As such, at approximately 11 mol% Sn, the direct and indirect piezoelectric properties become seemingly decoupled. In other words, while the domains in BTSn11 appear highly mobile, they seem to struggle to maintain a reoriented polarized state. Moreover, considering the number of P_{S} vector directions of the single phases can further help to understand the domain wall dynamics. The P_{S} vector should have 8 different directions in R, 12 in O, and 6 in T phase.[79] As mentioned above, BT should be at the O–T, BTSn3 in O, BTSn7 at the R–O, and BTSn11 in R at room temperature. Therefore, the number of P_{S} vector directions should be around 18, 12, 20, and 8 for BT, BTSn3, BTSn7, and BTSn11, respectively. By increasing the number of directions, the domain wall motion of the non-180° domain walls should be enhanced through creating a larger strain.[79] For BTSn7, the highest number of directions is found, which reflects the highest d_{33}. In general, for a maximized d_{33} a balance of reversible and irreversible contributions is necessary.

Overall, it can be assumed that by controlling the Sn concentration, the reversible and irreversible contributions to the dielectric response can be adjusted. However, the definition of the linear Rayleigh region strongly affects the extracted contributions, making them highly sensitive to Sn content and the applied electric field. Therefore, careful selection of this region is essential. These findings and trends on the impact of Sn doping on the irreversible and reversible contributions in BT highlight the importance of Rayleigh analysis, as the results can be correlated with electromechanical properties and are also essential for linking the trends observed in

microscopy methods to achieve a comprehensive understanding of domain structure dynamics.

Conclusion

It was shown that combining spectral imaging techniques with domain structure and domain wall dynamics analysis is a powerful tool for better understanding structure–property relationships in Sn-doped $BaTiO_3$. Structural measurements revealed a transition towards the cubic structure with increasing Sn-content, which corresponded with a decrease in grain size. Importantly, Mössbauer spectroscopy confirmed that Sn remains in the +4 oxidation state on the B-site, while XAFS indicated that Sn maintains a constant local environment with Sn–O $\approx$ 2.06 Å. These changes were marked by a significant change in the domain size and morphology, where PFM and Raman spectroscopy both displayed a reduction in the domain size and shape as well as an increase in the domain wall density. Interestingly, correlating the structural features with the spectroscopic signal revealed a good agreement between the polycrystalline and single-crystal $BaTiO_3$ analysis for the lamellar-type domains. The Sn-doped samples showed more complexity due to their irregular domain shapes, and with higher doping content and smaller domain sizes, it was increasingly challenging to resolve structural differences. The gradual increase in complexity and transformation of domain structures, as well as the reduction in domain size with increasing Sn content, correlates well with the observed increase in domain wall dynamics from the Rayleigh analysis. Furthermore, by investigating the real permittivity at small electric field amplitudes, an increase in both reversible and irreversible contributions with rising Sn content, together with the highest percentage of irreversible contributions around 11 mol% Sn, was observed. Hence, by adjusting the Sn concentration in $BaTiO_3$, the irreversible contributions can be tuned, which can be essential for the manufacturing of multimodal energy conversion systems.

Author contributions

V. Kraft: conceptualization (lead); data curation (equal); formal analysis (equal); investigation (equal); methodology (equal); project administration (equal); visualization (lead); writing – original draft (lead); writing – review & editing (lead). M. R. Cicconi: data curation (equal); formal analysis (equal); visualization (supporting); writing – original draft (supporting); writing – review & editing (supporting). S. Pal: data curation (equal); formal analysis (equal); visualization (supporting); writing – review & editing (supporting). M. Kuhfuß: formal analysis (supporting); writing – review & editing (supporting). N. H. Khansur: formal analysis (supporting); writing – review & editing (supporting). A. Martin: writing – original draft (supporting); writing – review & editing (supporting). K. Kimura: data curation (supporting); project administration (supporting); writing – review & editing (supporting); supervision (supporting). Y. Takabayashi: formal analysis (supporting); writing – review & editing (supporting). K. Mibu: data curation (supporting); formal analysis (supporting); funding acquisition (equal); methodology (equal); resources (equal); writing – review & editing (supporting). K. Hayashi: funding acquisition (equal); supervision (supporting); writing – review & editing (supporting). J. Briscoe: resources (supporting); supervision (supporting); writing – review & editing (supporting). Kyle G. Webber: conceptualization (supporting); formal analysis (supporting); funding acquisition (lead); project administration (lead); resources (lead); supervision (lead); writing – original draft (supporting); writing – review & editing (supporting).

Conflicts of interest

There are no conflicts to declare.

Data availability

The data supporting this article has been included as supplementary information (SI). Supplementary information: images and analysis of the measurements. See DOI: **https://doi.org/10.1039/d5tc03390j**.

Any additional raw data associated with this study is available upon request to the corresponding author.

Acknowledgements

References

1 N. P. M. J. Raj, G. Khandelwal and S.-J. Kim, *Nano Energy*, 2021, **83**, 105848.

2 A. Megdich, M. Habibi, L. Laperrière, Z. Li and Y. Abdin, *Mater. Today Sustainable*, 2024, **27**, 100847.

3 Z. Wang, Z. Liu, G. Zhao, Z. Zhang, X. Zhao, X. Wan, Y. Zhang, Z. L. Wang and L. Li, *ACS Nano*, 2022, **16**, 1661–1670.

4 H. Xu, G. Bai, S. Afzal, K. He, Z. Xiao, S. Yuan, Z. Lu, Q. Zhu and S. Xu, *J. Colloid Interface Sci.*, 2023, **651**, 705–713.

5 Y. Bai, J. Palosaari, P. Tofel and J. Juuti, *Energy Technol.*, 2020, **8**, 2000461.

6 Y. Zhang, X. Li, Q. He, M. Hameed and J. Briscoe, *Nano Energy*, 2025, **141**, 111120.

7 J. Huang, C. Jiang, M. An, P. Hu, Y. Xie, L. Li and Y. Chen, *Smart Mater. Struct.*, 2024, **33**, 065011.

8 Y. Bai, G. Vats, J. Seidel, H. Jantunen and J. Juuti, *Adv. Mater.*, 2018, **30**, 1803821.

9 ed. L. R. Thoutam, J. Ajayan and D. Nirmal, *Energy harvesting and storage devices: sustainable materials and methods*, CRC Press, Boca Raton, 1st edn, 2023.

10 X. Yang, Z. Yang, X. Wang, Y. Guo, Y. Xie, W. Yao and H. Kawasaki, *Appl. Mater. Today*, 2024, **40**, 102419.

11 X. Pan, Y. Wu, Y. Wang, G. Zhou and H. Cai, *Chem. Eng. J.*, 2024, **497**, 154249.

12 B. Xie, Y. Xie, Y. Ma, N. Luo, T. Xiang, C. Chin, D. Wang, F. Wang, B. Li, G. Jiang and X. Li, *ACS Appl. Electron. Mater.*, 2025, **7**, 185–192.

13 X. Lin, F. Yu, X. Zhang, W. Li, Y. Zhao, X. Fei, Q. Li, C. Yang and S. Huang, *ACS Appl. Nano Mater.*, 2023, **6**, 11955–11965.

14 R. Nechache, C. Harnagea, S. Li, L. Cardenas, W. Huang, J. Chakrabartty and F. Rosei, *Nat. Photonics*, 2015, **9**, 61–67.

15 I. Fina, C. Paillard and B. Dkhil, Photoferroelectric oxides, *arXiv*, 2017, preprint, arXiv:1709.09202, DOI: **10.48550/arXiv.1709.09202**.

16 J. Guo, Q. Zhang, D. Gai, L. Yang, W. Liang and C. Zhang, in *2024 IEEE 14th International Conference on CYBER Technology in Automation*, Control, and Intelligent Systems (CYBER), IEEE, Copenhagen, Denmark, 2024, pp. 638–643.

17 X. Long, H. Tan, F. Sánchez, I. Fina and J. Fontcuberta, *Nat. Commun.*, 2021, **12**, 382.

18 Z. Wang, C. Tan, M. Peng, Y. Yu, F. Zhong, P. Wang, T. He, Y. Wang, Z. Zhang, R. Xie, F. Wang, S. He, P. Zhou and W. Hu, *Light: Sci. Appl.*, 2024, **13**, 277.

19 I. Grinberg, D. V. West, M. Torres, G. Gou, D. M. Stein, L. Wu, G. Chen, E. M. Gallo, A. R. Akbashev, P. K. Davies, J. E. Spanier and A. M. Rappe, *Nature*, 2013, **503**, 509–512.

20 B. I. Sturman and V. M. Fridkin, *The photovoltaic and photorefractive effects in noncentrosymmetric materials*, Routledge, London, 2021.

21 Y. Bai, H. Jantunen and J. Juuti, *ChemSusChem*, 2019, **12**, 2540–2549.

22 S. Pal, S. Muthukrishnan, B. Sadhukhan, N. V. Sarath, D. Murali and P. Murugavel, *J. Appl. Phys.*, 2021, **129**, 084106.

23 S. Pal, A. B. Swain, P. P. Biswas and P. Murugavel, *Phys. Rev. Mater.*, 2020, **4**, 064415.

24 A. B. Swain, D. Murali, B. R. K. Nanda and P. Murugavel, *Phys. Rev. Appl.*, 2019, **11**, 044007.

25 J. Su and J. Zhang, *J. Mater. Sci.: Mater. Electron.*, 2019, **30**, 1957–1975.

26 D. Wang, Z. Fan, G. Rao, G. Wang, Y. Liu, C. Yuan, T. Ma, D. Li, X. Tan, Z. Lu, A. Feteira, S. Liu, C. Zhou and S. Zhang, *Nano Energy*, 2020, **76**, 104944.

27 Y. Yao, C. Zhou, D. Lv, D. Wang, H. Wu, Y. Yang and X. Ren, *Europhys. Lett.*, 2012, **98**, 27008.

28 V. Kraft, U. R. Eckstein, N. H. Khansur, F. P. Marlton, B. Mullens, A. Martin, K. Hayashi and K. G. Webber, *J. Am. Ceram. Soc.*, 2025, DOI: **10.1111/jace.70233**.

29 A. K. Kalyani, K. Brajesh, A. Senyshyn and R. Ranjan, *Appl. Phys. Lett.*, 2014, **104**, 252906.

30 W. Liu, J. Wang, X. Ke and S. Li, *J. Alloys Compd.*, 2017, **712**, 1–6.

31 W. Liu and X. Ren, *Phys. Rev. Lett.*, 2009, **103**, 257602.

32 F. Jona, G. Shirane and G. Shirane, *Ferroelectric crystals*, Dover Publ, New York, NY, Republ., 1993.

33 C. Lei, A. A. Bokov and Z.-G. Ye, *J. Appl. Phys.*, 2007, **101**, 084105.

34 P. Ren, Z. Liu, Q. Wang, B. Peng, S. Ke, H. Fan and G. Zhao, *Sci. Rep.*, 2017, **7**, 6693.

35 Y. Tan, G. Viola, V. Koval, C. Yu, A. Mahajan, J. Zhang, H. Zhang, X. Zhou, N. V. Tarakina and H. Yan, *J. Eur. Ceram. Soc.*, 2019, **39**, 2064–2075.

36 T. Shi, L. Xie, L. Gu and J. Zhu, *Sci. Rep.*, 2015, **5**, 8606.

37 L. Jin, F. Li and S. Zhang, *J. Am. Ceram. Soc.*, 2014, **97**, 1–27.

38 J. Schultheiß, G. Picht, J. Wang, Y. A. Genenko, L. Q. Chen, J. E. Daniels and J. Koruza, *Prog. Mater. Sci.*, 2023, **136**, 101101.

39 D. M. Evans, V. Garcia, D. Meier and M. Bibes, *Phys. Sci. Rev.*, 2020, **5**, 20190067.

40 A. Bhatnagar, A. Roy Chaudhuri, Y. Heon Kim, D. Hesse and M. Alexe, *Nat. Commun.*, 2013, **4**, 2835.

41 L. L. Ding, E. Beyreuther, B. Koppitz, K. Kempf, J. H. Ren, W. J. Chen, M. Rüsing, Y. Zheng and L. M. Eng, *Appl. Phys. Lett.*, 2024, **124**, 252901.

42 H. Matsuo, Y. Kitanaka, R. Inoue, Y. Noguchi, M. Miyayama, T. Kiguchi and T. J. Konno, *Phys. Rev. B*, 2016, **94**, 214111.

43 J. C. Yang, C. H. Yeh, Y. T. Chen, S. C. Liao, R. Huang, H. J. Liu, C. C. Hung, S. H. Chen, S. L. Wu, C. H. Lai, Y. P. Chiu, P. W. Chiu and Y. H. Chu, *Nanoscale*, 2014, **6**, 10524–10529.

44 F. Rubio-Marcos, A. Del Campo, P. Marchet and J. F. Fernández, *Nat. Commun.*, 2015, **6**, 6594.

45 J. Seidel, D. Fu, S.-Y. Yang, E. Alarcón-Lladó, J. Wu, R. Ramesh and J. W. Ager, *Phys. Rev. Lett.*, 2011, **107**, 126805.

46 M. Alexe, *Nano Lett.*, 2012, **12**, 2193–2198.

47 G. F. Nataf and M. Guennou, *J. Phys.: Condens. Matter*, 2020, **32**, 183001.

48 Z. Jiang, J. Huang, R. Yuan, N. Xu, Y. Jiang, J. Zhang, F. Zhang, J. Xing, H. Gu and D. Fu, *Phys. Status Solidi A*, 2022, **219**, 2200344.

49 H. Zhang, H. Giddens, T. G. Saunders, M. Palma, I. Abrahams, H. Yan and Y. Hao, *J. Eur. Ceram. Soc.*, 2024, **44**, 1627–1635.

50 N. Horchidan, A. C. Ianculescu, C. A. Vasilescu, M. Deluca, V. Musteata, H. Ursic, R. Frunza, B. Malic and L. Mitoseriu, *J. Eur. Ceram. Soc.*, 2014, **34**, 3661–3674.

51 Y. Tan, J. Zhang, Y. Wu, C. Wang, V. Koval, B. Shi, H. Ye, R. McKinnon, G. Viola and H. Yan, *Sci. Rep.*, 2015, **5**, 9953.

52 J. Gao, Y. Wang, Y. Liu, X. Hu, X. Ke, L. Zhong, Y. He and X. Ren, *Sci. Rep.*, 2017, **7**, 40916.

53 P. Lagos L, R. Hermans Z, N. Velasco, G. Tarrach, F. Schlaphof, C. Loppacher and L. M. Eng, *Surf. Sci.*, 2003, **532–535**, 493–500.

54 P. S. Dobal and R. S. Katiyar, *J. Raman Spectrosc.*, 2002, **33**, 405–423.

55 M. Deluca, H. Hu, M. N. Popov, J. Spitaler and T. Dieing, *Commun. Mater.*, 2023, **4**, 78.

56 ed. J. Toporski, T. Dieing and O. Hollricher, *Confocal Raman Microscopy*, Springer International Publishing, Cham, 2018, vol. 66.

57 ed. A. Zoubir, *Raman Imaging: Techniques and Applications*, Springer Berlin Heidelberg, Berlin, Heidelberg, 2012, vol. 168.

58 M. Deluca, L. Stoleriu, L. P. Curecheriu, N. Horchidan, A. C. Ianculescu, C. Galassi and L. Mitoseriu, *J. Appl. Phys.*, 2012, **111**, 084102.

59 Y. Wang, Y. B. Liu, X. H. Hu, Y. T. He, J. H. Gao and L. S. Zhong, *2017 1st International Conference on Electrical Materials and Power Equipment (ICEMPE)*, IEEE, Xi'an, China, 2017, pp. 507–510.

60 B. Ravel and M. Newville, *J. Synchrotron Radiat.*, 2005, **12**, 537–541.

61 D. K. Dobesh, A. Gadelmawla, H. Miyazaki, M. Hinterstein, K. Kimura, J. G. Maier, S. Banerjee, O. Zeair, S. C. Mehta, L. L. Da Silva, N. H. Khansur, K. Hayashi, D. De Ligny, K. G. Webber and M. R. Cicconi, *J. Eur. Ceram. Soc.*, 2024, **44**, 5646–5658.

62 R. D. Shannon, *Acta Crystallogr. Sect. A*, 1976, **32**, 751–767.

63 M. J. Hoffmann, M. Hammer, A. Endriss and D. C. Lupascu, *Acta Mater.*, 2001, **49**, 1301–1310.

64 Y.-H. Seo, D. J. Franzbach, J. Koruza, A. Benčan, B. Malič, M. Kosec, J. L. Jones and K. G. Webber, *Phys. Rev. B: Condens. Matter Mater. Phys.*, 2013, **87**, 094116.

65 H. Elangovan, M. Barzilay, J. Huang, S. Liu, S. Cohen and Y. Ivry, *ACS Nano*, 2021, **15**, 13380–13388.

66 G. M. Dalpian, Q. Liu, C. C. Stoumpos, A. P. Douvalis, M. Balasubramanian, M. G. Kanatzidis and A. Zunger, *Phys. Rev. Mater.*, 2017, **1**, 025401.

67 Y. Huang, C. Zhao, B. Wu and X. Zhang, *J. Eur. Ceram. Soc.*, 2022, **42**, 2764–2771.

68 K. C. Singh, A. K. Nath, R. Laishram and O. P. Thakur, *J. Alloys Compd.*, 2011, **509**, 2597–2601.

69 D. Shihua, S. Tianxiu, Y. Xiaojing and L. Guanghua, *Ferroelectrics*, 2010, **402**, 55–59.

70 L. Chen, Q. Fu, Z. Jiang, J. Xing, Y. Gu, F. Zhang, Y. Jiang and H. Gu, *J. Eur. Ceram. Soc.*, 2021, **41**, 7654–7661.

71 T. O'Reilly, K. Holsgrove, A. Gholinia, D. Woodruff, A. Bell, J. Huber and M. Arredondo, *Acta Mater.*, 2022, **235**, 118096.

72 G. Arlt and P. Sasko, *J. Appl. Phys.*, 1980, **51**, 4956–4960.

73 A. L. Kholkin, D. A. Kiselev, I. K. Bdikin, A. Sternberg, B. Dkhil, S. Jesse, O. Ovchinnikov and S. V. Kalinin, *Materials*, 2010, **3**, 4860–4870.

74 G. Pezzotti, K. Okai and W. Zhu, *J. Appl. Phys.*, 2012, **111**, 013504.

75 J. Schultheiß, S. Checchia, H. Uršič, T. Frömling, J. E. Daniels, B. Malič, T. Rojac and J. Koruza, *J. Eur. Ceram. Soc.*, 2020, **40**, 3965–3973.

76 H. H. Wieder, *Phys. Rev.*, 1955, **99**, 1161–1165.

77 V. Kraft, S. Spreafico, M. R. Cicconi, M. Kuhfuß, K. Mibu, K. Kimura, K. Hayashi, V. A. Balanov, Y. Bai, N. H. Khansur, B. Meyer and K. G. Webber, *J. Appl. Phys.*, 2025, **138**, 094104.

78 R. E. Eitel, in *2007 Sixteenth IEEE International Symposium on the Applications of Ferroelectrics*, 2007, pp. 319–323.

79 Y. Huan, X. Wang, L. Li and J. Koruza, *Appl. Phys. Lett.*, 2015, **107**, 202903.

80 R. Placeres-Jiménez, J. P. Rino and J. A. Eiras, *J. Phys. Appl. Phys.*, 2015, **48**, 035304.

81 L. Rayleigh, *Lond. Edinb. Dublin Philos. Mag. J. Sci.*, 1887, **23**, 225–245.

82 D. Damjanovic and M. Demartin, *J. Phys.: Condens. Matter*, 1997, **9**, 4943.

83 D. Damjanovic, *J. Appl. Phys.*, 1997, **82**, 1788–1797.

84 L. Mitoseriu and L. P. Curecheriu, *Nanoscale Ferroelectrics and Multiferroics*, John Wiley & Sons, Ltd, 2016, pp. 473–511.

85 Y. Ding, T. Zheng, C. Zhao and J. Wu, *J. Appl. Phys.*, 2019, **126**, 124101.

86 Y. Cheng, J. Xing, X. Li, L. Xie, Y. Xie, Z. Tan and J. Zhu, *J. Am. Ceram. Soc.*, 2022, **105**, 5213–5221.

87 I. A. Atito, H. T. Shaban, A. Salem, M. Ezzeldien and A. E. Mahmoud, *J. Korean Ceram. Soc.*, 2022, **59**, 705–714.

88 B. Peng, Z. Yue and L. Li, *J. Appl. Phys.*, 2011, **109**, 054107.

89 G. E. Eyoum, U. Eckstein, K. Riess, A. Gadelmawla, E. Springer, K. G. Webber and N. H. Khansur, *J. Mater. Sci.*, 2022, **57**, 15843–15861.